PHYSICAL REVIEW B **107**, L081405 (2023)

Letter

Shear-strain controlled high-harmonic generation in graphene

Tomohiro Tamaya,[1,2,*] Hidefumi Akiyama,[1] and Takeo Kato[1]
[1]*Institute for Solid State Physics, University of Tokyo, Kashiwa 277-8581, Japan*
[2]*JST, PRESTO, 4-1-8 Honcho, Kawaguchi, Saitama 332-0012, Japan*

(Received 3 January 2023; revised 9 February 2023; accepted 13 February 2023; published 28 February 2023)

We propose a method for controlling the high-harmonic generation (HHG) with a high dynamic range in single-layer graphene. We find that, by utilizing shear strain, a significant enhancement or quenching of HHG is possible over a range of several orders of magnitude. This feature is made possible by the resonance mechanism at a van Hove singularity. Therein, the shear strain controls the configurations of the two Dirac cones, resulting in changes in the energy and dipole moment at the saddle point of the band dispersion. Our findings provide a way for modulating or switching light by using a nano-optomechanical device composed of single-layer graphene.

DOI: 10.1103/PhysRevB.107.L081405

Two-dimensional (2D) Dirac electrons in single-layer graphene have attracted much attention [1,2] for their novel linear and nonlinear optical properties [3–30]. One-atom-thick graphene exhibits universal frequency-independent light absorption, $\pi\alpha = 2.3\%$, where $\alpha = e^2/\hbar c \simeq 1/137$ is the fine structure constant [3–10]. Ultrafast carrier dynamics on massless bands provide a variety of high-speed broadband optical responses [11,12] which include saturable absorption enabling stable passive mode locking [13–18], light emission [19,20], detection [21,22], and modulation [23,24]. Giant optical nonlinearity [25] and high-harmonic generation (HHG) [26,27] have also been reported, which indicate intriguing strong light-matter interactions in graphene in the visible, infrared, and terahertz (THz) regions.

Further studies have targeted artificial control, modulation, or switching of these properties for potential applications in graphene-based optical devices [23,26,27,31–35]. Indeed, modulation of the HHG intensity has been demonstrated over a range of two orders of magnitude via tuning of the Fermi energy by gate voltage [26] or via tuning of the incident-light ellipticity [27]. However, the robustness of optical transition probability $\pi\alpha$ inherent to 2D Dirac electrons makes the external control of optical responses highly challenging, and a significant modification of the Dirac band dispersion should be necessary to achieve giant switching of optical responses.

A graphene sheet has high flexibility and a shear strain of up to 27% can be reversibly applied to it [36–58]. Notably, a few theoretical studies [55–58] have pointed out that shear strain in graphene makes the two Dirac cones at the $K^{\pm}$ points to get closer and finally merge to form a band gap. This strain effect should be useful for control of the nonlinear optical responses of graphene.

In this Letter, we theoretically demonstrate a significant enhancement or quenching of HHG over several orders of magnitude in graphene by tuning the shear strain and the incident-light polarization angle. We clarify that the enhancement stems from the resonance between the incident-light photon energy and the band-gap or saddle-point energies at the intermediate point of the two Dirac cones. High-contrast control of the nonlinearity suggests the possibility of using HHG-light switching and modulation in graphene photonics and optoelectronics.

The graphene under shear strain can be modeled by a tight-binding model based on a distorted hexagonal lattice [see Fig. 1(a)]. The anisotropic hopping energies are described as $\gamma_i \approx \gamma_0 e^{\beta(|\boldsymbol{\delta}'_i| a_0^{-1} - 1)}$ by considering changes of the distance between neighboring $2p_z$ atomic orbitals. Here, we set γ_0 to be the hopping energy for unstrained graphene and chose β to be 3.37 [42,43]. The displacement vectors from the initial to neighboring sites are described as $\boldsymbol{\delta}'_1 = (1/2 - \sqrt{3}\zeta/2, -\sqrt{3}/2 + \zeta/2)a$, $\boldsymbol{\delta}'_2 = (1/2 + \sqrt{3}\zeta/2, \sqrt{3}/2 + \zeta/2)a$, and $\boldsymbol{\delta}'_3 = (-1, -\zeta)a$, respectively, where ζ and a are the shear-strain parameter and lattice constant of unstrained graphene.

HHG in shear-strained graphene is formulated by an extended theoretical framework based on the previous ones [27,59–63]. The theoretical framework employed here is based on the tight-binding model that is known to provide quantitatively reasonable results for the band structures of shear-strained graphene [55–57]. We suppose the vector potential of the incident THz light to be $\boldsymbol{A}(t) = A_0 f(t)\cos(\omega_0 t)\boldsymbol{n}$, where $f(t)$ is the envelope function of the incident pulse, $\boldsymbol{n} = (\cos\theta, \sin\theta)$ is a unit vector pointing in the direction of the electric field, and θ is the tilt angle measured from the armchair axis [see Fig. 1(a)]. We chose $f(t) = (t - t_0)^2/\tau^2$ to be the envelope function, where $t_0 = 24\pi/\omega_0$ and $\tau = 4\pi/\omega_0$. The tight-binding Hamiltonian on a distorted honeycomb lattice in momentum space can be expressed as (see Supplemental Material Sec. I [64])

$$H = \sum_{\boldsymbol{k}} (e_{\boldsymbol{k}}^{\dagger}\ h_{-\boldsymbol{k}}) \begin{pmatrix} \xi(\boldsymbol{k}, t) & \eta(\boldsymbol{k}, t) \\ \eta(\boldsymbol{k}, t)^{*} & -\xi(\boldsymbol{k}, t) \end{pmatrix} \begin{pmatrix} e_{\boldsymbol{k}} \\ h_{-\boldsymbol{k}}^{\dagger} \end{pmatrix}, \qquad (1)$$

---

[*] tamaya@g.ecc.u-tokyo.ac.jp

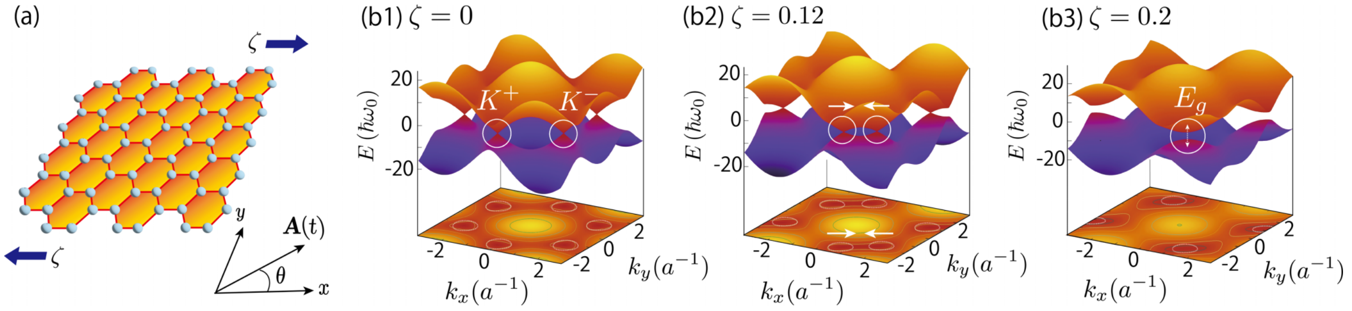

FIG. 1. (a) Schematic figure of lattice structure of graphene under shear strain. The amplitude of the shear strain is represented by ζ and the vector potential of the incident light is denoted as $\boldsymbol{A}(t)$, whose tilt angle measured from the armchair axis is described by θ (see the inset). (b1)–(b3) Variation in band structures of graphene for the three shear-strain parameters: (b1) $\zeta = 0$, (b2) $\zeta = 0.12$, and (b3) $\zeta = 0.2$. The white arrows in (b2) indicate the direction of the change in position of the Dirac points induced by the strain.

where $e_{\boldsymbol{k}}$ ($h_{\boldsymbol{k}}$) is the annihilation operator of electrons (holes) with wave number $\boldsymbol{k}$, $\xi(\boldsymbol{k},t) = |f(\boldsymbol{k})| + \hbar\,\mathrm{Re}[\Omega_R^*(\boldsymbol{k},t)e^{i\theta_{\boldsymbol{k}}}]$, $\eta(\boldsymbol{k},t) = -\hbar\,\mathrm{Im}[\Omega_R^*(\boldsymbol{k},t)e^{i\theta_{\boldsymbol{k}}}]$, $f(\boldsymbol{k}) = \sum_{i=1}^{3} \gamma_i e^{i\boldsymbol{k}\cdot\boldsymbol{\delta}_i'} = |f(\boldsymbol{k})|$ $e^{i\theta_{\boldsymbol{k}}}$, and $\Omega_R(\boldsymbol{k},t) = \boldsymbol{d}(\boldsymbol{k})\cdot\boldsymbol{A}(t)$ is the Rabi frequency defined from the $\boldsymbol{k}$-dependent dipole vector $\boldsymbol{d}(\boldsymbol{k}) = (d_x^{\boldsymbol{k}}, d_y^{\boldsymbol{k}})$ [the explicit form of the dipole moment $\boldsymbol{d}(\boldsymbol{k})$ is given in the Supplemental Material Sec. I [64]]. We solved the time-dependent equations for polarizations and carrier densities derived from the Hamiltonian, and evaluated the HHG intensity spectra by performing a Fourier transformation on the generated current [65]. In this work, we only focused on HHG emitted along the major axis [parallel to $\boldsymbol{A}(t)$] and ignored the perpendicular component [62] due to its complex behavior as a function of the incident-light polarization angle and THz frequency.

Figure 1 shows the three-dimensional (3D) plot (upper figures) and contour plot (projection figures) of the band structure for three different shear-strain parameters, $\zeta = 0$ [Fig. 1(b1)], $\zeta = 0.12$ [Fig. 1(b2)], and $\zeta = 0.2$ [Fig. 1(b3)]. For unstrained graphene ($\zeta = 0$), we can see that Dirac cones exist at the $K^{\pm}$ points indicated by the white circles in Fig. 1(b1). These two Dirac cones gradually get closer to each other as the shear-strain parameter increases [see Fig. 1(b2)], and consequently, they merge and an energy gap appears [see Fig. 1(b3)]. In our tight-binding model, the critical strength of the shear strain for a band gap to form is estimated as $\zeta_c \approx 0.165$, which is consistent with previous works [55,66].

The shear-strain dependences of the third and fifth harmonics are shown in Figs. 2(a1) and 2(b1) for an incident-light frequency of $\omega_0 = 90$ THz. The red and green lines indicate the dependences for the different incident-light polarization angles, $\theta = 120^\circ$ and $\theta = 30^\circ$, respectively. These two angles are regarded as the specific ones because they can yield the maximum and minimum intensities of the emitted harmonics [see the insets in Figs. 2(a1) and 2(b1)]. Figures 2(a1) and 2(b1) show that, for $\theta = 120^\circ$, the third-order (fifth-order) harmonics are largely enhanced by around one order of magnitude at $\zeta \approx 0.13$ and 0.18, while they are quenched rapidly by around third (eight) orders of magnitude at $0.2 < \zeta < 0.27$ (red line). The plots for $\theta = 30^\circ$ do not show this nonmonotonic behavior; they only show an approximately monotonic decrease with increasing shear strain. Figures 2(a2) and 2(b2) show the shear-strain dependence of the third- and fifth-order harmonics for the different incident-light frequencies, $\omega_0 = 30$ THz (blue lines), 60 THz (orange lines), 90 THz (red lines), and 120 THz (green lines). Here, the interval between the two peaks grows with increasing incident-light frequency. This result suggests that HHG should be enhanced when the photon energy of the incident light coincides with a characteristic energy in the electronic structure.

Strong incident-light polarization angle dependence is another remarkable feature of HHG in strained graphene [see Figs. 2(a1) and 2(b1)]. This feature reflects the fact that the distribution of the excited carriers is sensitive to the

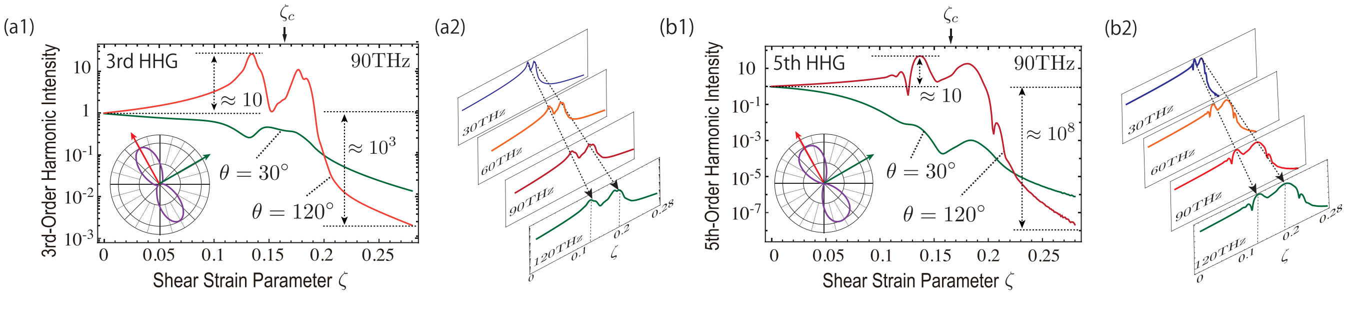

FIG. 2. (a1) and (b1) Shear-strain dependence of the third- and fifth-order harmonics for $\omega_0 = 90$ THz. The red and green lines indicate the high-harmonic intensities for the incident-light angles $\theta = 120^\circ$ and $\theta = 30^\circ$, respectively. The polarization angle dependences of the third and fifth harmonics for $\zeta = 0.12$ are shown in the insets. The critical strength of the shear strain for a band gap to form is described by ζ_c. (a2) and (b2) Shear-strain dependence of the third- and fifth-order harmonics for the different incident-light frequencies, 30 THz (blue lines), 60 THz (orange lines), 90 THz (red lines), and 120 THz (green lines). The dotted black arrows indicate the variation in the double peaks.

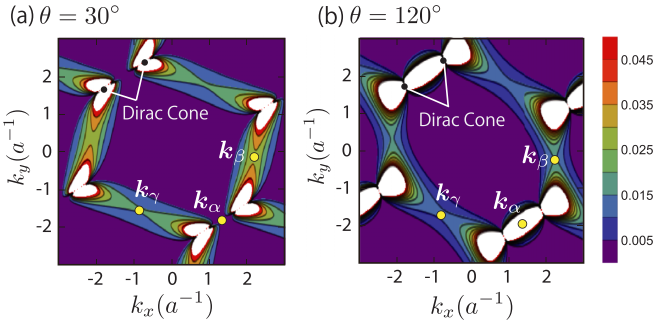

FIG. 3. Contour plots of distribution of carrier density in $\boldsymbol{k}$ space after photoirradiation. The incident-light polarization angle is (a) $\theta = 30°$ and (b) $\theta = 120°$. The shear-strain parameter and incident-light frequency are $\zeta = 0.12$ and $\omega_0 = 90$ THz.

polarization angle of the incident light. Figures 3(a) and 3(b) show the distributions of the carrier density in $\boldsymbol{k}$ space after photoirradiation for $\theta = 30°$ and $\theta = 120°$. Here, we set the shear-strain parameter and the incident-light frequency as $\zeta = 0.12$ and $\omega_0 = 90$ THz, respectively. In these figures, the positions of the three saddle points of the band dispersion, $\boldsymbol{k}_\alpha$, $\boldsymbol{k}_\beta$, and $\boldsymbol{k}_\gamma$, are indicated by yellow points, and those of the two Dirac cones are denoted by black points. We find that the carrier density near the saddle point $\boldsymbol{k}_\alpha$ is suppressed for $\theta = 30°$ while it is enhanced for $\theta = 120°$. This fact indicates that the polarization angle of the incident light mainly affects the carrier excitation near the saddle point $\boldsymbol{k}_\alpha$.

To better understand these features, we will investigate the characteristics of THz light absorption in shear-strained graphene. On the basis of linear response theory [67], we can derive the absorption coefficient $\alpha(\omega)$ as (see Supplemental Material Sec. III [64])

$$\alpha(\omega) \simeq \frac{\pi}{\hbar\omega}\sum_{\boldsymbol{k}}\left(\beta_x^{\boldsymbol{k}}\cos\theta + \beta_y^{\boldsymbol{k}}\sin\theta\right)^2 \times [\delta(\omega - 2\epsilon_{\boldsymbol{k}}) - \delta(\omega + 2\epsilon_{\boldsymbol{k}})], \qquad (2)$$

where $\beta_x^{\boldsymbol{k}}$ and $\beta_y^{\boldsymbol{k}}$ are defined as $\beta_i^{\boldsymbol{k}} = -c\hbar(\mathrm{Im}[d_i^{\boldsymbol{k}}]\cos\theta_{\boldsymbol{k}} - \mathrm{Re}[d_i^{\boldsymbol{k}}]\sin\theta_{\boldsymbol{k}})$ $(i = x, y)$. Figure 4(a) shows the frequency dependence of the absorption coefficients for the three different incident-light polarization angles, $\theta = 30°$ (green line), 95° (blue line), and 120° (red line) in the case of $\zeta = 0.12$. These plots show that each peak originates from a singularity in the density of state (DOS), i.e., a van Hove singularity (vHS), which is induced by the saddle points of the band dispersion in $\boldsymbol{k}$ space. Figure 4(b) is a contour plot of the band dispersion $\epsilon_{\boldsymbol{k}} = |f(\boldsymbol{k})|$ for $\zeta = 0.12$ as well as its saddle point. The carrier excitations near the three saddle points, labeled $\boldsymbol{k}_\alpha$, $\boldsymbol{k}_\beta$, and $\boldsymbol{k}_\gamma$, induce the peak structures denoted as vHS$_\alpha$, vHS$_\beta$, and vHS$_\gamma$ in Fig. 4(a). Figure 4(b) also shows that each saddle

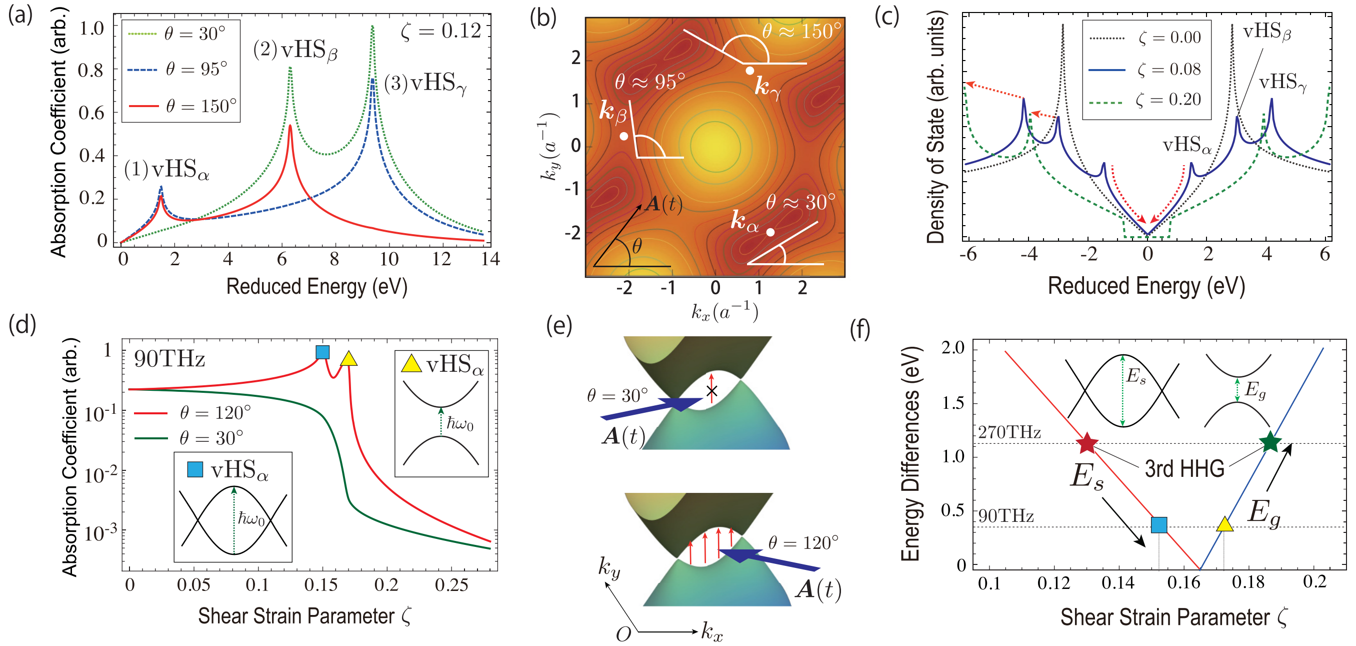

FIG. 4. (a) Absorption coefficients of graphene for $\zeta = 0.12$. The green, blue, and red lines show those for different incident-light polarization angles $\theta = 30°$, $\theta = 95°$, and $\theta = 120°$, respectively. Each peak corresponds to different vHSs, induced by the saddle points at $\boldsymbol{k}_\alpha$, $\boldsymbol{k}_\beta$, and $\boldsymbol{k}_\gamma$ shown in (b). (b) Contour plot of the energy band in graphene for $\zeta = 0.12$. Here, $\boldsymbol{k}_\alpha$, $\boldsymbol{k}_\beta$, and $\boldsymbol{k}_\gamma$ indicate the positions of the saddle points in $\boldsymbol{k}$ space, each of which induces vHS$_\alpha$, vHS$_\beta$, and vHS$_\gamma$, respectively. The azimuth angle toward the band minima (the Dirac cones) measured from the saddle points are indicated by the white lines. (c) DOS of graphene for the different shear-strain parameters, $\zeta = 0$ (black dotted line), $\zeta = 0.12$ (blue line), and $\zeta = 0.2$ (green dashed line). The red lines indicate that vHS shifts with increasing shear strain. (d) Absorption coefficients of graphene as a function of the shear-strain parameter ζ. The red and blue lines indicate those for the incident-light polarization angles $\theta = 120°$ and $\theta = 30°$. The insets show the resonant mechanisms corresponding to the double peaks of the red line (blue square and yellow triangles). (e) Schematic figure of photon absorption near vHS$_\alpha$ for different incident-light polarization angles $\theta = 30°$ (upper figure) and $\theta = 120°$ (lower figure). (f) Energy differences at vHS$_\alpha$ (E_s) and the band-gap energy E_g as a function of shear strain. The blue square and yellow triangle indicate the resonant points marked in Fig. 4(d).

point has a different angle to the band minima (the Dirac points) that can be estimated as $\theta \approx 30^\circ$, $\theta \approx 95^\circ$, and $\theta \approx 150^\circ$ [see the white lines in Fig. 4(b)]. We can identify that the peaks observed in Fig. 4(a) disappear when the direction of the incident light matches these angles, while the peak height in the absorption coefficient becomes a maximum when the incident light is perpendicular to them (see Supplemental Material Sec. IV [64]). Thus, the vHS peaks in the absorption coefficient significantly depend on the relation between the polarization angle of the incident light and the band structure. The position of the vHSs in DOS changes depending on the strength of the shear strain. Figure 4(c) plots the DOS of graphene for $\zeta = 0$ (black dotted line), $\zeta = 0.08$ (blue line), and $\zeta = 0.2$ (green dashed line). In the absence of shear strain ($\zeta = 0$), only one vHS can be seen in the positive (negative) energy region. Applying shear strain splits it into three peaks (in each region) by breaking the energy degeneracy of the vHSs. The lowest-energy peak, labeled vHS$_\alpha$, moves toward zero energy with increasing ζ (the blue line and the red curved arrow), and consequently, it reaches zero and the band gap starts to form (the green line). At the same time, the other two peaks, denoted by vHS$_\beta$ and vHS$_\gamma$, monotonically move toward the high-energy region (the red straight arrows). These numerical results imply that the properties of HHG in the THz regime ($\hbar\omega_0 \ll 1$ eV) would be governed by the behavior of vHS$_\alpha$.

Next, we focus on the absorption coefficient in the THz regime. Figure 4(d) plots the shear-strain dependence of the absorption coefficient for $\theta = 120^\circ$ (red line) and $\theta = 30^\circ$ (green line) in the case of $\omega_0 = 90$ THz. This figure indicates that the absorption coefficient has two peaks for $\theta = 120^\circ$, whereas the plot for $\theta = 30^\circ$ only shows a monotonic decrease. These tendencies are very similar to those of the HHG in Figs. 2(a1) and 2(b1). As discussed so far, the properties of these peaks can be understood in terms of the relation between the incident-light polarization angle and vHS$_\alpha$ [see Fig. 4(e)]. Note that this angular dependence comes from the dependence of the dipole moment $\boldsymbol{d}_i^{\boldsymbol{k}}$ on $\boldsymbol{k}$ through the coefficient $\beta_x^{\boldsymbol{k}} \cos\theta + \beta_y^{\boldsymbol{k}} \sin\theta$ in Eq. (2). The electron-hole excitation energy at vHS$_\alpha$ (E_s) and the band gap (E_g) are plotted as a function of the shear-strain parameter ζ in Fig. 4(f). Comparing Figs. 4(d) and 4(f), we can conclude that the first peak in Fig. 4(d) (the blue square) should appear when the incident-light energy matches E_s (see the lower inset), while the second peak (the yellow triangle) should appear when it matches E_g (see the upper inset). This analysis enables us to conclude that the two HHG peaks in Figs. 2(a1) and 2(b1) arise from resonant conditions, $3\hbar\omega_0 = E_s$ and $3\hbar\omega_0 = E_g$, as indicated by the red and green star marks in Fig. 4(f). Note that the orientation of the dipole moment does not change much between before and after the energy gap forming. Thus, we can conclude that the significant enhancement in HHG is caused by the resonant mechanism at $\boldsymbol{k}_\alpha$ that changes greatly depending on the polarization angle of the incident light.

So far, we have demonstrated that application of shear strain on graphene enables a significant control of HHG over several orders of magnitude. Note that it is fundamentally different from HHG modifications via control of carrier-envelope phase or chirp. The former controls material responses directly, while the latter use controlled incident light via some other methods. Therefore, our method provides a unique way for modulating or switching HHG of THz waves with a high dynamic range, which should be necessary in near-future high-speed wireless communication. A single-layer graphene may simultaneously solve problems of cost, mass, and volume of materials for an application of THz technology.

In conclusion, we theoretically investigated the linear and nonlinear optical responses of graphene distorted by shear strain. Using the tight-binding model, we clarified that tuning both the shear strain and the polarization angle of the incident THz light enables a significant enhancement or quenching of HHG. By using linear response theory, we showed that the HHG enhancement came from the resonances at which the incident-light photon energy matches the saddle-point energy or the band gap. In addition, the dipole moment near the saddle point (or the band gap) plays an important role in the polarization angle dependence of this enhancement. Strong quenching of HHG was induced by rapid growth of the band-gap energy with increasing shear strain. Our findings suggest the possibility of using shear strain to control HHG in graphene and pave the way for optical nanotechnology of single-layer materials.

The authors acknowledge the support from the Japan Society for the Promotion of Science (JSPS KAKENHI Grants No. JP19K14624, No. JP20K03831, and No. JP21H01361) and JST PRESTO (JPMJPR2107).

---

[1] K. S. Novoselov, A. K. Geim, S. V. Morozov, D.-e. Jiang, Y. Zhang, S. V. Dubonos, I. V. Grigorieva, and A. A. Firsov, Science **306**, 666 (2004).

[2] A. H. Castro Neto, F. Guinea, N. M. R. Peres, K. S. Novoselov, and A. K. Geim, Rev. Mod. Phys. **81**, 109 (2009).

[3] R. R. Nair, P. Blake, A. N. Grigorenko, K. S. Novoselov, T. J. Booth, T. Stauber, N. M. Peres, and A. K. Geim, Science **320**, 1308 (2008).

[4] T. Ando, Y. Zheng, and H. Suzuura, J. Phys. Soc. Jpn. **71**, 1318 (2002).

[5] V. P. Gusynin, S. G. Sharapov, and J. P. Carbotte, Phys. Rev. Lett. **96**, 256802 (2006).

[6] S.-E. Zhu, S. Yuan, and G. Janssen, Europhys. Lett. **108**, 17007 (2014).

[7] K. F. Mak, M. Y. Sfeir, Y. Wu, C. H. Lui, J. A. Misewich, and T. F. Heinz, Phys. Rev. Lett. **101**, 196405 (2008).

[8] L. Yang, J. Deslippe, C.-H. Park, M. L. Cohen, and S. G. Louie, Phys. Rev. Lett. **103**, 186802 (2009).

[9] Y. Cai, J. Zhu, and Q. H. Liu, Appl. Phys. Lett. **106**, 043105 (2015).

[10] L. Falkovsky and A. Varlamov, Eur. Phys. J. B **56**, 281 (2007).

[11] M. Baudisch, A. Marini, J. D. Cox, T. Zhu, F. Silva, S. Teichmann, M. Massicotte, F. Koppens, L. S. Levitov, F. J. García de Abajo *et al.*, Nat. Commun. **9**, 1018 (2018).

[12] F. Bonaccorso, Z. Sun, T. Hasan, and A. Ferrari, Nat. Photonics **4**, 611 (2010).

[13] Z. Sun, T. Hasan, F. Torrisi, D. Popa, G. Privitera, F. Wang, F. Bonaccorso, D. M. Basko, and A. C. Ferrari, ACS Nano **4**, 803 (2010).

[14] Q. Bao, H. Zhang, Y. Wang, Z. Ni, Y. Yan, Z. X. Shen, K. P. Loh, and D. Y. Tang, Adv. Funct. Mater. **19**, 3077 (2009).

[15] N. Vermeulen, D. Castelló-Lurbe, M. Khoder, I. Pasternak, A. Krajewska, T. Ciuk, W. Strupinski, J. Cheng, H. Thienpont, and J. Van Erps, Nat. Commun. **9**, 2675 (2018).

[16] Z. Sun, D. Popa, T. Hasan, F. Torrisi, F. Wang, E. J. Kelleher, J. C. Travers, V. Nicolosi, and A. C. Ferrari, Nano Res. **3**, 653 (2010).

[17] A. Martinez, K. Fuse, and S. Yamashita, Appl. Phys. Lett. **99**, 121107 (2011).

[18] J. Ma, G. Xie, P. Lv, W. Gao, P. Yuan, L. Qian, H. Yu, H. Zhang, J. Wang, and D. Tang, Opt. Lett. **37**, 2085 (2012).

[19] C. H. Lui, K. F. Mak, J. Shan, and T. F. Heinz, Phys. Rev. Lett. **105**, 127404 (2010).

[20] Y. D. Kim, Y. Gao, R.-J. Shiue, L. Wang, B. Aslan, M.-H. Bae, H. Kim, D. Seo, H.-J. Choi, S. H. Kim *et al.*, Nano Lett. **18**, 934 (2018).

[21] F. Xia, T. Mueller, Y.-m. Lin, A. Valdes-Garcia, and P. Avouris, Nat. Nanotechnol. **4**, 839 (2009).

[22] X. Gan, R.-J. Shiue, Y. Gao, I. Meric, T. F. Heinz, K. Shepard, J. Hone, S. Assefa, and D. Englund, Nat. Photonics **7**, 883 (2013).

[23] M. Liu, X. Yin, E. Ulin-Avila, B. Geng, T. Zentgraf, L. Ju, F. Wang, and X. Zhang, Nature (London) **474**, 64 (2011).

[24] W. Li, B. Chen, C. Meng, W. Fang, Y. Xiao, X. Li, Z. Hu, Y. Xu, L. Tong, H. Wang *et al.*, Nano Lett. **14**, 955 (2014).

[25] E. Hendry, P. J. Hale, J. Moger, A. K. Savchenko, and S. A. Mikhailov, Phys. Rev. Lett. **105**, 097401 (2010).

[26] G. Soavi, G. Wang, H. Rostami, D. G. Purdie, D. De Fazio, T. Ma, B. Luo, J. Wang, A. K. Ott, D. Yoon *et al.*, Nat. Nanotechnol. **13**, 583 (2018).

[27] N. Yoshikawa, T. Tamaya, and K. Tanaka, Science **356**, 736 (2017).

[28] Y. M. Chang, H. Kim, J. H. Lee, and Y.-W. Song, Appl. Phys. Lett. **97**, 211102 (2010).

[29] M. Cizmeciyan, J. Kim, S. Bae, B. H. Hong, F. Rotermund, and A. Sennaroglu, Opt. Lett. **38**, 341 (2013).

[30] R. Denk, M. Hohage, P. Zeppenfeld, J. Cai, C. A. Pignedoli, H. Söde, R. Fasel, X. Feng, K. Müllen, S. Wang *et al.*, Nat. Commun. **5**, 4253 (2014).

[31] T. Otsuji, S. B. Tombet, A. Satou, H. Fukidome, M. Suemitsu, E. Sano, V. Popov, M. Ryzhii, and V. Ryzhii, J. Phys. D **45**, 303001 (2012).

[32] Y. Zhao, X.-g. Li, X. Zhou, and Y.-n. Zhang, Sens. Actuators, B **231**, 324 (2016).

[33] V. Singh, D. Joung, L. Zhai, S. Das, S. I. Khondaker, and S. Seal, Prog. Mater. Sci. **56**, 1178 (2011).

[34] Q.-Y. Wen, W. Tian, Q. Mao, Z. Chen, W.-W. Liu, Q.-H. Yang, M. Sanderson, and H.-W. Zhang, Sci. Rep. **4**, 7409 (2014).

[35] A. N. Grigorenko, M. Polini, and K. Novoselov, Nat. Photonics **6**, 749 (2012).

[36] Z. Peng, X. Chen, Y. Fan, D. J. Srolovitz, and D. Lei, Light: Sci. Appl. **9**, 190 (2020).

[37] O. Frank, M. Mohr, J. Maultzsch, C. Thomsen, I. Riaz, R. Jalil, K. S. Novoselov, G. Tsoukleri, J. Parthenios, K. Papagelis *et al.*, ACS Nano **5**, 2231 (2011).

[38] A. Castellanos-Gomez, V. Singh, H. S. van der Zant, and G. A. Steele, Ann. Phys. **527**, 27 (2015).

[39] S. Bertolazzi, J. Brivio, and A. Kis, ACS Nano **5**, 9703 (2011).

[40] A. Castellanos-Gomez, M. Poot, G. A. Steele, H. S. Van Der Zant, N. Agraït, and G. Rubio-Bollinger, Adv. Mater. **24**, 772 (2012).

[41] J. Shi and L. Q. Chen, J. Appl. Phys. **125**, 082201 (2019).

[42] V. M. Pereira and A. H. Castro Neto, Phys. Rev. Lett. **103**, 046801 (2009).

[43] R. Ribeiro, V. M. Pereira, N. Peres, P. Briddon, and A. C. Neto, New J. Phys. **11**, 115002 (2009).

[44] J. Zhao, G.-Y. Zhang, and D.-X. Shi, Chin. Phys. B **22**, 057701 (2013).

[45] E. Cadelano, P. L. Palla, S. Giordano, and L. Colombo, Phys. Rev. Lett. **102**, 235502 (2009).

[46] C. Lee, X. Wei, J. W. Kysar, and J. Hone, Science **321**, 385 (2008).

[47] F. Liu, P. Ming, and J. Li, Phys. Rev. B **76**, 064120 (2007).

[48] Z. H. Ni, T. Yu, Y. H. Lu, Y. Y. Wang, Y. P. Feng, and Z. X. Shen, ACS Nano **2**, 2301 (2008).

[49] S.-M. Choi, S.-H. Jhi, and Y.-W. Son, Phys. Rev. B **81**, 081407(R) (2010).

[50] S.-H. Bae, Y. Lee, B. K. Sharma, H.-J. Lee, J.-H. Kim, and J.-H. Ahn, Carbon **51**, 236 (2013).

[51] H. Tian, Y. Shu, Y.-L. Cui, W.-T. Mi, Y. Yang, D. Xie, and T.-L. Ren, Nanoscale **6**, 699 (2014).

[52] F. Guinea, Solid State Commun. **152**, 1437 (2012).

[53] V. M. Pereira, A. H. Castro Neto, and N. M. R. Peres, Phys. Rev. B **80**, 045401 (2009).

[54] G. Gui, J. Li, and J. Zhong, Phys. Rev. B **78**, 075435 (2008).

[55] G. Cocco, E. Cadelano, and L. Colombo, Phys. Rev. B **81**, 241412(R) (2010).

[56] C. Si, Z. Sun, and F. Liu, Nanoscale **8**, 3207 (2016).

[57] Y. Li, X. Jiang, Z. Liu, and Z. Liu, Nano Res. **3**, 545 (2010).

[58] I. I. Naumov and A. M. Bratkovsky, Phys. Rev. B **84**, 245444 (2011).

[59] T. Tamaya, A. Ishikawa, T. Ogawa, and K. Tanaka, Phys. Rev. Lett. **116**, 016601 (2016).

[60] T. Tamaya, A. Ishikawa, T. Ogawa, and K. Tanaka, Phys. Rev. B **94**, 241107(R) (2016).

[61] T. Tamaya and T. Kato, Phys. Rev. B **100**, 081203(R) (2019).

[62] T. Tamaya and T. Kato, Phys. Rev. B **103**, 205202 (2021).

[63] P. Xia, T. Tamaya, C. Kim, F. Lu, T. Kanai, N. Ishii, J. Itatani, H. Akiyama, and T. Kato, Phys. Rev. B **104**, L121202 (2021).

[64] See Supplemental Material at http://link.aps.org/supplemental/10.1103/PhysRevB.107.L081405 for detailed information on our theoretical framework and additional numerical data supporting our arguments.

[65] Our theoretical framework is consistent with the previous ones [68,69] in the limit of $\zeta = 0$. To confirm the validity of this framework, we also checked that the exotic characteristics of HHG identified in the past experiment were reproduced (see Supplemental Material Sec. II [64]).

[66] I. Y. Sahalianov, T. M. Radchenko, V. A. Tatarenko, G. Cuniberti, and Y. I. Prylutskyy, J. Appl. Phys. **126**, 054302 (2019).

[67] R. Kubo, J. Phys. Soc. Jpn. **12**, 570 (1957).

[68] E. Malic, T. Winzer, E. Bobkin, and A. Knorr, Phys. Rev. B **84**, 205406 (2011).

[69] T. Stroucken, J. H. Grönqvist, and S. W. Koch, Phys. Rev. B **84**, 205445 (2011).